



HAL
open science

Numerical and experimental study of supersonically expanding argon plasma using a micrometer hollow cathode discharge

Y Gu, Nicolas Suas-David, Jordy Bouwman, Yongdong Li, Harold Linnartz

► **To cite this version:**

Y Gu, Nicolas Suas-David, Jordy Bouwman, Yongdong Li, Harold Linnartz. Numerical and experimental study of supersonically expanding argon plasma using a micrometer hollow cathode discharge. *Journal of Applied Physics*, 2024, 135 (19), pp.193302. 10.1063/5.0207234 . hal-04599942

HAL Id: hal-04599942

<https://hal.science/hal-04599942v1>








Submitted on 4 Jun 2024

HAL is a multi-disciplinary open access archive for the deposit and dissemination of scientific research documents, whether they are published or not. The documents may come from teaching and research institutions in France or abroad, or from public or private research centers.

L'archive ouverte pluridisciplinaire **HAL**, est destinée au dépôt et à la diffusion de documents scientifiques de niveau recherche, publiés ou non, émanant des établissements d'enseignement et de recherche français ou étrangers, des laboratoires publics ou privés.

RESEARCH ARTICLE | MAY 17 2024

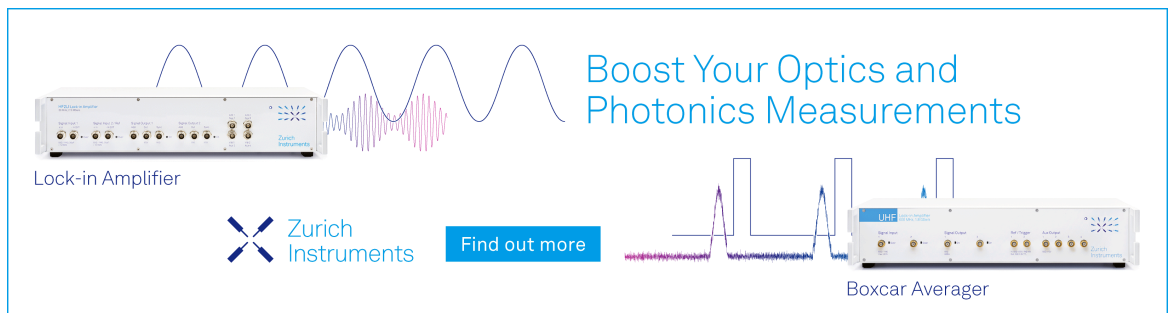
Numerical and experimental study of supersonically expanding argon plasma using a micrometer hollow cathode discharge

Yu Gu ; Nicolas Suas-David  ; Jordy Bouwman ; Yongdong Li  ; Harold Linnartz 



J. Appl. Phys. 135, 193302 (2024)

<https://doi.org/10.1063/5.0207234>



Boost Your Optics and Photonics Measurements

Lock-in Amplifier

Zurich Instruments

Find out more

Boxcar Averager

Numerical and experimental study of supersonically expanding argon plasma using a micrometer hollow cathode discharge

Cite as: J. Appl. Phys. 135, 193302 (2024); doi: 10.1063/5.0207234

Submitted: 6 March 2024 · Accepted: 2 May 2024 ·

Published Online: 17 May 2024



Yu Gu,^{1,2}  Nicolas Suas-David,^{2,3,a)}  Jordy Bouwman,^{2,4,5,6}  Yongdong Li,^{1,a)}  and Harold Linnartz² 

AFFILIATIONS

¹Key Laboratory of Physical Electronics and Devices of Ministry of Education, Faculty of Electronic and Information Engineering, Xi'an Jiaotong University, Xi'an 710049, China

²Laboratory for Astrophysics, Leiden Observatory, Leiden University, 9513, RA Leiden 2300, The Netherlands

³Institut de Physique de Rennes—UMR 6251, Univ Rennes, CNRS, Rennes F-35000, France

⁴Laboratory for Atmospheric and Space Physics, University of Colorado, Boulder, Colorado 80303, USA

⁵Department of Chemistry, University of Colorado, Boulder, Colorado 80309, USA

⁶Institute for Modeling Plasma, Atmospheres, and Cosmic Dust (IMPACT), University of Colorado, Boulder, Colorado 80303, USA

^{a)}Authors to whom correspondence should be addressed: nicolas.suas-david@univ-rennes.fr and leyond@mail.xjtu.edu.cn

ABSTRACT

Pulsed discharge nozzles (PDNs) have been successfully used for decades to produce rotationally cold ($T_{\text{rot}} \sim 20$ K) radicals and ions of astrophysical interest and to characterize these species spectroscopically. In this work, an evolution of the PDN, the piezostack pulsed discharge nozzle (P²DN), is used for the first time to investigate the characteristics of the still poorly understood supersonic plasma expansion. The P²DN allows for a better control of the reservoir pressure of which an accurate measurement is required to characterize the plasma expansion. This new source, thus, gives the opportunity to further optimize the plasma conditions and extend its use to new target species. The spatial distribution of an argon plasma and the effect of the supersonic flow for different pressures are studied by combining a two-dimensional extended fluid model (extFM) and a direct simulation Monte Carlo (DSMC) method. The combined simulation is validated with experimental results obtained through emission spectroscopy associated with a group-code collisional-radiative model to retrieve the plasma parameters. The validated numerical approach (DSMC-extFM) allows for an accurate characterization of the plasma structure in our typical experimental conditions (a reservoir pressure ranging from 90 to 905 mbar). Thus, this simulation will be used in future studies to improve the plasma conditions to favor the synthesis of (transient) hydrocarbon species as found in space, by seeding the argon gas with a suitable precursor, such as acetylene.

© 2024 Author(s). All article content, except where otherwise noted, is licensed under a Creative Commons Attribution (CC BY) license (<https://creativecommons.org/licenses/by/4.0/>). <https://doi.org/10.1063/5.0207234>

I. INTRODUCTION

Supersonic planar plasma sources have opened new experimental possibilities for spectroscopic studies of transient species of astrophysical interest. These systems combine several advantages: (i) an effective adiabatic cooling resulting in low final rotational temperatures ($T_{\text{rot}} \sim 20$ K), (ii) a setting that allows (nearly) Doppler free spectroscopy, (iii) relatively long absorption path lengths, determined by the slit length, typically between 2.5 and 7.5 cm, and (iv) a negligible transversal velocity that does not

substantially affect the line shape (compared to a circular orifice). Typical radical and ion densities amount to 10^{10} and 10^{12} particles/cm³. This all helps in increasing overall detection sensitivities. Over the years, different planar plasma configurations have been designed, using laser photolysis, electron impact, and high voltage discharge configurations and applying different direct absorption techniques, varying from plasma (double) modulation up to cavity ring down (CRDS) or broad band cavity enhanced spectroscopy (CEAS).^{1–10} Although all these nozzles have been proven to

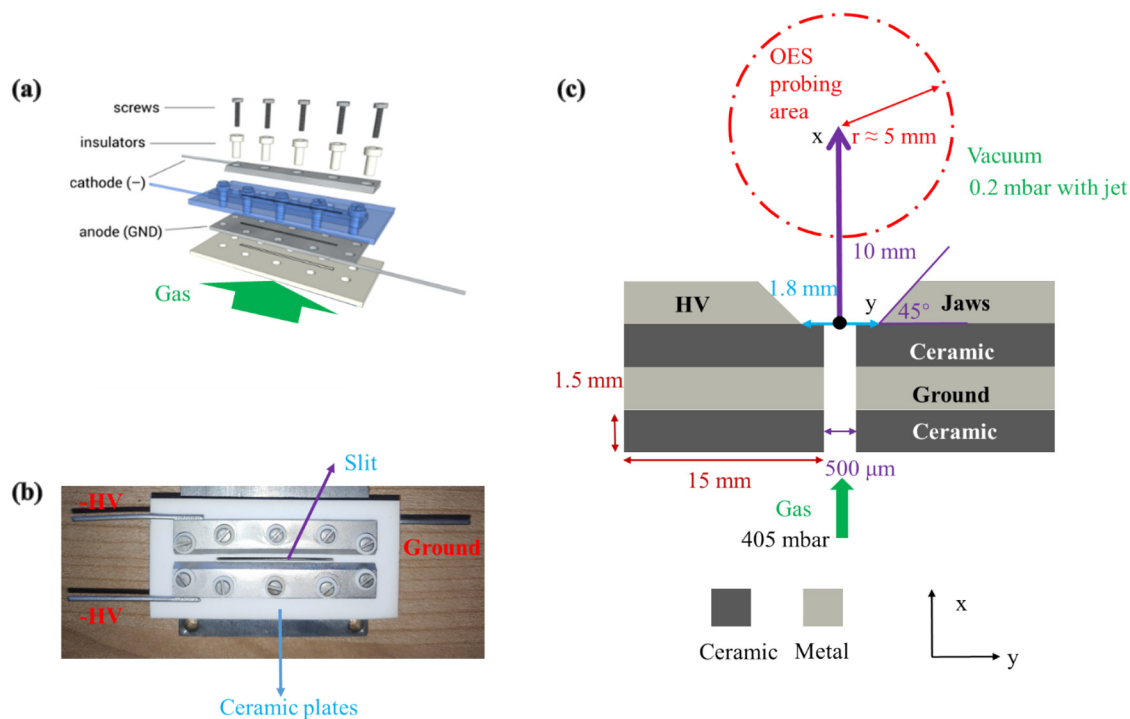
04 June 2024 07:58:53

be very useful sources for molecular spectroscopy, covering UV/VIS to FIR and MW with applications ranging from carbon chain radicals and ionic complexes to PAH cations and rovibrationally or vibronically excited molecules and transients (see, e.g., Refs. 11–15), to our knowledge, only few efforts have been made to physically characterize the involved plasma processes.^{4,16–18} To achieve efficient adiabatic cooling, the precursor is seeded in a carrier gas, such as argon, helium, nitrogen, etc. This inert species is in large excess (usually around 99%) and is, therefore, the main contributor in triggering and sustaining the plasma.

The present study focuses on describing the plasma processes at play in one of the most used supersonic planar plasma discharge nozzles to date. This P²DN, an updated version of the PDN configuration introduced by Motylewski and Linnartz nearly 25 years ago,⁵ uses a negative high voltage discharge pulse of a premixed gas in a micrometer hollow cathode configuration, just before the gas can expand (Fig. 1). Over the years, a large number of carbon chain radicals have been studied, using this system, typically discharging mixtures of C₂H₂ and/or C₂N₂ in He or Ar. In the plasma, the precursor species is dissociated and the formed reactive intermediates (i.e., CH, CN, CH₂, C₂H₂⁺, C₂ and C₂⁻, etc.) recombine in the expansion, resulting in the synthesis of species like C₃, C₆H, HC₈H⁺, C₉H₃⁺, or NC₆N⁺ (see, e.g., Refs. 19–21).

The term commonly used in literature for such thin slit (=hollow) devices is a “micro-hollow cathode discharge” (MHCD)

because of the characteristic geometry defined by a few hundred micrometers hollow width.²² MHCD studies are working with a quasi-stagnation gas and are considered to operate in two possible discharge configuration: glow or hollow mode²³ depending on the gas pressure, hollow size, and bias voltage. To model a micro-hollow discharge plasma, numerous approaches are nowadays available: Particle in cell (PIC),^{24,25} PIC-MCC (particle in cell-Monte Carlo collision),^{25,26} plasma fluid,^{27–29} and global models.^{30,31} Experimentally, it is much harder to investigate the plasma inside the hollow because of its small size, which makes it difficult to access, even with a focused laser beam, but information can be retrieved from studying the plasma expanding downstream. Here, we will focus on the plasma characteristics of the P²DN shown in Fig. 1. The only other plasma simulation study^{16–18} looking in more depth into a similar system used a plasma fluid model. This numerical study found that within the nozzle, charged species show a maximum between the insulator plate and the flow axis. It was concluded that their setup named, PDN (plasma discharge nozzle), runs as a glow discharge in the abnormal regime. The influence of different dielectric thicknesses with same bias voltage was investigated, and in a follow-up study, the results revealed that increasing the inter-electrode distance does not significantly influence the plasma distribution.³² This previous work focused on the simulation and optimization of the cathode–anode area ignoring the supersonic expansion region, which is the region that is probed



04 June 2024 07:58:53

FIG. 1. (a) A three-dimensional schematic, (b) a photo, and (c) a schematic 2D cross section of the P²DN nozzle. The latter provides the parameters used for the simulations: Materials and dimensions of the electrodes and ceramic (insulating) parts, typical pressures along with the position and the area that is probed spectroscopically (red dotted circle labelled OES that stands for “Optical Emission Spectroscopy”).

to record spectra. In the present study, the expansion is explicitly considered, and this additional information highlights the conditions within the isentropic core of the expansion and will be used to validate the numerical approach that aims to model the whole source.

To explicitly link the research fields of laboratory astrophysics and plasma studies, we want to highlight that P²DN is a micro-hollow cathode discharge (MHCD) coupled with supersonic expansion. Compared to widespread MHCD experiments, this system differs through its high velocity flow and resulting distribution of ions and electrons. The primary goal here is to study the P²DN argon plasma characteristics, and this is achieved by a combination of modeling effort and experimental work. The retrieved plasma jet properties from the numerical model are validated by interpreting emission spectra using an argon collisional radiative (CR) model. Similar jet structures were diagnosed by absorption spectroscopy in a previous paper,¹⁸ but the ionization rate and, in particular, the density associated with P²DN did not satisfy the physical assumptions behind a Boltzmann fitting. The homemade CR model developed here is based on Zhu *et al.*,³³ which has been used for different applications, such as an electron beam plasma (EBP),³³ an inductively coupled plasma (ICP),³⁴ a capacitive coupled plasma (CCP),³⁵ and a microwave micro-plasma (called split-ring resonator or SRR).³⁶ While this specific CR model has never been applied to a supersonic expansion, other approaches have been reported for a supersonic argon plasma jet (see, e.g., Kano *et al.*).³⁷

The article is organized as follows. First, we will describe the new P²DN plasma source used in this work. Next, we will discuss the simulations of the gas expansion (DSMC) and the modeling of the argon plasma characteristics (extFM). Subsequently, the results of the simulations of our supersonic expansion are presented, followed by numerical results on the plasma characteristics. The spectrometer and the recorded argon plasma emission spectra will be presented next, followed by a description of the collisional-radiative (CR) model that is used to extract the electron temperature and electron density from the experimental data. We end by drawing conclusions on the comparisons of the numerical model and the experimental data.

II. GAS PULSE AND PLASMA SOURCE

The P²DN is based on a design introduced in the 1990s⁵ and for which the pulsed gas inlet has been upgraded for the present work. A high throughput piezoelectric stack valve injects efficiently a high mass flow into a reservoir coupled with a fast pressure transducer.³⁸ The system is fed with typically 4 bar (up to 25 bar) backing pressure of argon gas (Linde 5.0). Backing pressures as high as 20 bar have been used. The valve is operated at 20 Hz, and gas pulses are set to last 1.2 ms. Subsequently, the gas expands through a metal body onto which the slit assembly is mounted. The slit assembly is shown as a 3D schematic in Fig. 1 and consists of a slotted grounded metal (anode), a slotted ceramic (dielectric) plate of 1.5 mm width insulating the anode from two metal jaws, acting as a cathode, that can be adjusted for tweaking the electromagnetic field intensity. The overall aperture of the output of the nozzle is $\sim 3 \text{ cm} \times 500 \mu\text{m}$. The plasma is generated inside the slit by striking a negative high-voltage discharge from jaws to the metal

plate. The slotted ceramic plate separates the cathode and anode. All plates are aligned by screws that are electrically isolated from the electrodes by ceramic tubing.

To discharge the argon gas, a pulsed high-voltage power supply is used and an equivalent 60 μF capacitor series is charged to negative 1400 V and connected to the jaws through a 2 k Ω ballast resistor. This limits the maximum current on the P²DN electrodes. Discharge pulses typically last 100–300 μs , i.e., substantially shorter than the opening time of the piezoelectric stack valve and a delay generator allows to optimize the discharge pulse along the gas pulse.

The P²DN is mounted in a high-vacuum chamber (an ISO-160 six-cross piece) that is evacuated by a roots blower system with a total pumping capacity around 1500 m³/h. During jet operation, the pressure in the vacuum chamber amounts to typically 0.2 mbar. The discharge nozzle is mounted onto an ISO-160 flange that contains all voltage and gas feedthroughs. Two other flanges define the optical axis, a few cm downstream of the nozzle orifice and parallel to the slit.

III. GAS SIMULATIONS AND PLASMA MODELING

The challenge in simulating the plasma processes in the P²DN system is in combining the properties of an abnormal glow discharge (MHCD) with those of an expanding flow. Decoupling the simulation in two distinct parts, however, is possible because of the very different time scales associated with the processes taking place in the hollow and in the expansion. The neutral gas velocity ($\sim 10^2$ m/s) is orders of magnitude slower than that of electrons ($\sim 10^6$ m/s) and even ions ($\sim 10^4$ m/s), and consequently, time scales characterizing the flow characteristics are considered nearly static compared to the plasma behavior of charged (and excited) species. Moreover, as the excited/ionized species represents only a fraction of the total number density of the flow, their influence (and, in particular, their high temperatures) on the overall supersonic expansion structure is considered to be negligible.

The gas expansion is simulated by a direct simulation Monte Carlo approach and the discharge by a plasma extended fluid model (extFM). This decoupling refrains from performing a time-dependent modeling of the formation of the plasma and instead focuses on a specific time, a snapshot, corresponding to our experimental measurements. In the following, we will refer to this regime as a fully developed plasma. Because of the large length/width ratio (~ 100) of the slit, the effect of the boundary layers can be neglected. Thus, a simple 2D model assuming a slit of infinite length is used as this further lowers the computational requirements for both simulations. All these simplifications have also been made in an earlier study presented in Ref. 17.

A. Simulating the gas expansion

Supersonic expansions are widely used in laboratories to adiabatically cool gas to very low (rotational and translational) temperatures (few Kelvins). This allows for recording spectra of molecular transients of astronomical interest as close as possible to typical astronomical conditions. Moreover, this comes with simplification of the spectrum as well as an increase in detection sensitivity.

04 June 2024 07:58:53

To model the plasma expansion produced during a single gas discharge pulse, it is important to know the density and kinetic temperature distribution. As we consider the plasma expansion fully developed while recording the spectra, only a snapshot of the involved thermodynamics is needed when the computation has converged. As supersonic expansions are characterized by a high Knudsen number, a computational fluid dynamics (CFD) analysis based on the Navier–Stokes conservation equations is not suited here. Instead, a direct simulation Monte Carlo (DSMC) method as developed by Bird can be used.^{39–42} More specifically, a recent set of fluid solvers has been collected under the name “Hystrath”⁴³ within the frame of the OpenFOAM-v1706 open source library.⁴⁴ These solvers focus on the hypersonic and rarefied flow. Among them, the dsmcFoam+⁴⁵ is a direct application of the DSMC approach, improving the default dsmcFoam solver in the OpenFOAM repository.

Our model starts 6 mm upstream from the output of the nozzle, including the whole diode geometry before expansion. The reservoir before the nozzle is not simulated in order to reduce the high-pressure region, which would increase the computational time by orders of magnitude. Furthermore, the full nozzle, that is to say the hollow and the jaws, is taken into account while only a limited part of the space in the vacuum chamber is simulated. The inlet boundary condition is mainly determined by the stagnation density, the whole nozzle (including the electrodes and the ceramics) is set as a wall, and a deletion patch is assigned to the limits of the vacuum chamber. The outlet boundary (the side perpendicular to the expansion) is linked to a density corresponding to the experimentally measured pressure. The structured mesh is typically composed by quadrilaterals cells of 100 μm side length. As described earlier, the ratio between the length and the width of the nozzle is large, and therefore, the nozzle width is considered infinite in the model. This simplification speeds up the calculation as one dimension can be discarded. In a similar way, only half of the expansion is computed given the existing mirror symmetry. A number of 10¹⁰ equivalent particles and time steps of 10^{−8} s are found to provide a realistic simulation of the expansion for a reasonable computational time.

B. Plasma model

Two different models, the PIC^{24–26} and the plasma fluid model,^{27–29} are commonly used to numerically study MCHD plasma in two dimensions. The PIC method is the main approach that can directly solve the Maxwell field and Newton–Lorentz motion equations by a finite difference together with a finite size-particle method⁴⁶ used to represent a set of actual charged particles.⁴⁷ The particle model considers the motion macro-particles, so it reflects the motion of the actual plasma best. However, in a long-term numerical simulation, the large number of particle motions leads irrevocably to a rapid increase in the calculation time. For our selected experiments, the plasma dynamics is not relevant as the spectrum in the non-steady regime is not captured by the spectrometer. This work only focuses on steady conditions. The plasma fluid model, on the contrary, studies the properties of plasma in a large spatial and temporal range from a macro perspective. Thus, here the latter model has been implemented as it offers a reliable

TABLE I. Collisions and reactions used in the plasma fluid model.

| Reaction | Formula | Type | Δε (eV) |
|----------|---|----------------------|---------|
| 1 | $e + \text{Ar} \rightarrow e + \text{Ar}$ | Elastic | 0 |
| 2 | $e + \text{Ar} \rightarrow e + \text{Ar}^*$ | Excitation | 11.5 |
| 3 | $e + \text{Ar}^* \rightarrow e + \text{Ar}$ | Superelastic | −11.5 |
| 4 | $e + \text{Ar} \rightarrow 2e + \text{Ar}^+$ | Ionization | 15.8 |
| 5 | $e + \text{Ar}^* \rightarrow 2e + \text{Ar}^+$ | Ionization | 4.24 |
| 6 | $\text{Ar}^* + \text{Ar}^* \rightarrow e + \text{Ar} + \text{Ar}^+$ | Penning ionization | ... |
| 7 | $\text{Ar}^* + \text{Ar}^* \rightarrow \text{Ar} + \text{Ar}$ | Metastable quenching | ... |

approximation associated with a reasonable calculation time. The plasma fluid model’s governing equations include the continuity equation of the particles, the electron energy balance equation, and the Poisson equation.⁴⁸ In this study, we use a two-dimensional self-consistent plasma extended fluid model⁴⁹ based on a finite elements method to simulate our plasma. The simulations are performed using COMSOL (6.1) multi-physics software through the plasma module.⁵⁰

In the simulations, two species are taken into account: electrons (e) and atomic argon in its ground (Ar), excited (Ar*), and cationic (Ar⁺) states. The excited Ar* represents the four levels in the 4s (1s according to Paschen notation) manifold of argon. The argon collisional reactions used in this work are listed in Table I. The electron energy distribution function (EEDF) is calculated by the two-term Boltzmann equation in each calculation time step.⁵¹

The nozzle dimensions have already been introduced in Fig. 1. The vacuum chamber simulation area is represented by a 12 × 30 mm rectangle. Only half of this area is actually computed as the expansion shows a symmetry plane along its axis. On the

04 June 2024 07:58:53

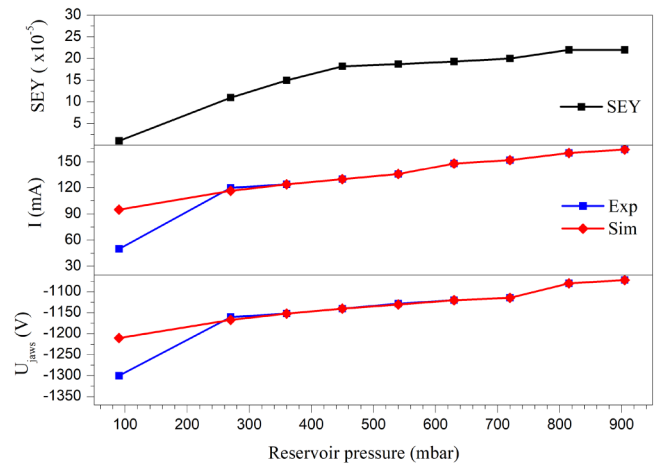


FIG. 2. Evolution of the SEY values set in our simulation (top panel) as a function of the reservoir pressure and the corresponding jaws’ currents (middle panel) and voltages (bottom panel).

y-axis, the size of the chamber is set to be the same as the jaw width of 15 mm. For the x-axis, the plasma expansion area is taken as 12 mm.

In addition to the internal mesh where the influence of both the plasma and the potential produced by the electrodes is taken into account, the jaws themselves are also considered where only the electrostatic solver is used. The surface of the cathode is set as a metal connected to the ballast resistor.

The ion-induced secondary electron yield (SEY) on the cathode surface depends on multiple factors, such as the reduced electric field E/n , discharge gas, and, in particular, the electrode material and its surface condition.^{52,53} Our electrodes are made of stainless steel. To our knowledge, there exists no accurate experimentally derived argon/stainless steel SEY in the operating range of our reduced electric field. In spite of a sharp pressure gradient along the cathode surface, SEY is set as a constant to simplify the calculation and is adjusted to retrieve the current density and voltage on the cathode to fit the experimental values. Thus, here the SEY is ranging between 1×10^{-5} and 2×10^{-4} depending on the reservoir pressure (see Fig. 2).

Figure 2 shows the numerical and experimental voltage and current evolution along with their associated SEY values as function of the reservoir pressure when maintaining a steady DC voltage at negative 1.4 kV. Experimentally, as expected, the current (I) increases linearly with the pressure while the voltage on the jaws (V) decreases with the reduction of the mean-free-path of electrons. Only the simulation associated with a reservoir pressure of 90 mbar diverges from this behavior, and this may be caused by a limitation of the fluid model to describe the discharge at low pressure.⁵⁴ For this specific case, the SEY has been determined by linearly extrapolating the values at higher pressure because there exists no suitable value to reproduce the current density under this condition. The rest of the simulated data is in very good agreement with the observational data.

Except for the cathode and the outlet, the rest of the boundaries are set to de-excite argon through collisions. The anode is grounded, and the vacuum chamber boundary is set to the Neumann condition to mimic a larger vacuum region. As discussed later in the article, this latter boundary condition may lead to an unrealistic electron density distribution in the vicinity of the limit of the mesh. However, its influence on the upstream measured area is expected to remain limited.

Due to the strong gradients of charged particles' density and fields' intensity inside the hollow, the mesh corresponding to the nozzle is denser than that of the chamber with a typical maximum cell length of 2×10^{-5} m compared to 2×10^{-4} m in the chamber. The whole mesh is built from ten thousands of quadrilateral cells. An electrostatic field solver, implemented in COMSOL software, is used to first calculate the electric field associated with electrons and ions of different energies. These electrons and ions are then used to compute the production of excited species according to their excitation energy reported in Table I. In turn, the newly produced ions influence the initial electric field distribution through the drift diffusion equation. This process is repeated at each time step, as summarized in Fig. 3, until the convergence criteria are reached, that is to say, when the residue of electron density is below 1 cm^{-3} .

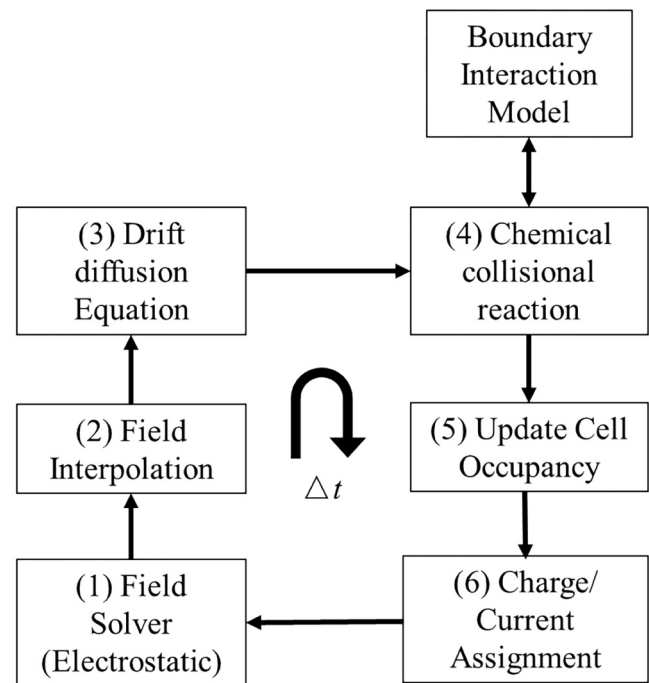


FIG. 3. Flow chart of the plasma fluid model used in this article.

IV. SIMULATION RESULTS

Besides the simulation of the P²DN plasma, the goal of this study is also to characterize the highest density regions of the different species involved in order to better understand chemical processes occurring in this system when hydrocarbons are injected alongside argon. To characterize the electron (e), ion (Ar^+), and excited argon (Ar^*) densities and temperature distributions, the plasma model described in Sec III B has been combined with the DSMC simulation as presented in Sec. III A. As we probe a quasi-steady plasma that is fully developed, the results presented in this section correspond to the situation when the time-dependent simulation has converged. In the following, only the simulation results for the expansion associated with a reservoir pressure of 450 mbar is presented. The different pressures used in this study (from 90 to 905 mbar) do not significantly modify the flow or the plasma structure in the region close to the nozzle output that we are studying. The main noticeable change arises from the different argon densities (and therefore their excited and ionized states form along with the electron densities) that can be basically scaled up or down from the 450 mbar reservoir pressure reference study presented below.

A. Supersonic expansion simulation results

The results of the simulation are shown in Fig. 4 and follow the use of the dsmcFoam+ solver⁴⁵ implemented within the OpenFOAM toolbox.⁴⁴ The upper panel shows the cross section of the nozzle and flow expansion, and the color coding indicates the

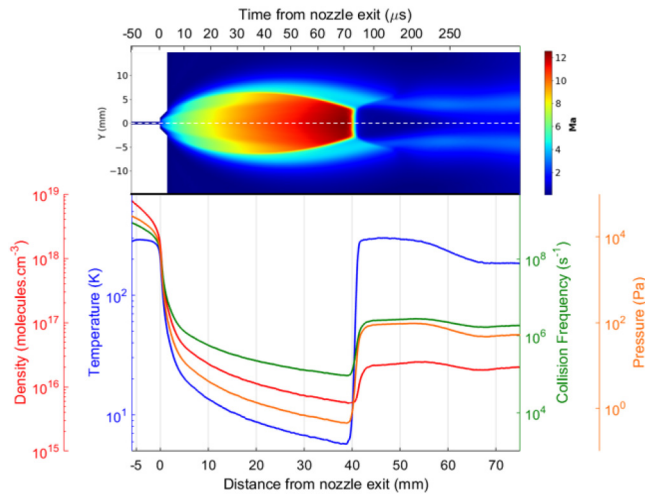


FIG. 4. Supersonic expansion modeling from a DSMC approach. The flow structure within the vacuum chamber is represented by the distribution of the Mach number (upper panel). The evolution of density (red), temperature (blue), collision rate (green), and pressure (orange) as a function of distance along the flow axis (represented as white dots in the upper panel) is plotted in the lower panel.

Mach number. The evolution of thermodynamical properties—density, temperature, collision frequency, and pressure—along the flow axis is shown in the lower panel. From this, it becomes clear that once the gas leaves the nozzle orifice, there is a steep drop in density and density-related properties, such as pressure and collision rate. The adiabatic nature of the expansion causes the kinetic temperature to drop below 10 K. At 10 mm from the output of the nozzle, corresponding to the center of area probed by our emission spectrometer, the density and the kinetic temperature are around $2 \times 10^{16} \text{ cm}^{-3}$ and 15 K, respectively. The behavior of the thermodynamical properties has been checked by comparison to DS2V software developed by the pioneer of the DSMC method³⁹ and empirical models.⁵⁵

As the excited/ionized species represent only a fraction of the neutral gas density, the overall structure of the modelled expansion is very similar to the real plasma expansion. Figure 5 highlights the region and the two thermodynamical parameters, the density and the kinetic temperature, used by the plasma model, whose outputs are represented in the following figures.

B. Plasma numerical results

1. Voltage potential (U), electrical field intensity (E), and reduced electrical field intensity (E/n)

In our experiments, the output voltage of the pulse power generator is set at -1400 V . The overall quasi-neutral plasma shows a locally positively charged region close to the electrodes called the cathode fall or plasma sheath.⁵⁶ This region is clearly visible on the 2D potential distribution in Fig. 6(a) as it corresponds to the absolute voltage drop in the chamber near the cathodes. The isovalues

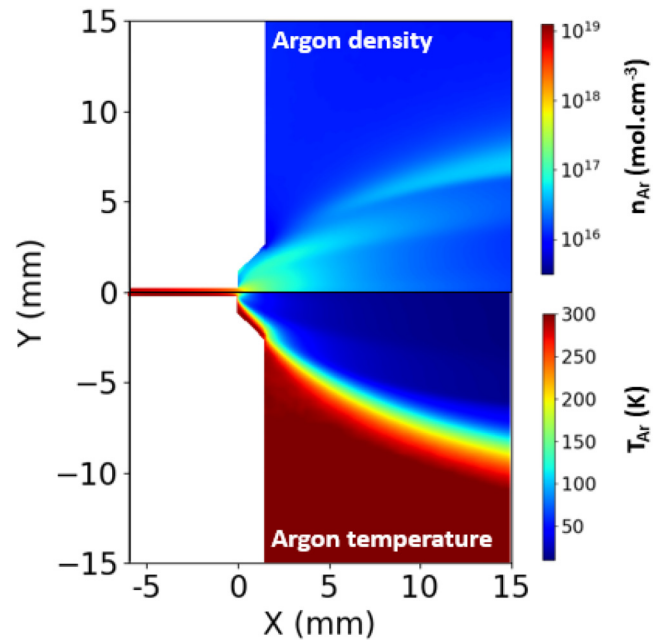


FIG. 5. Zoom-in on the flow simulation presented in Fig. 4 showing the region of interest for plasma modeling. The argon density distribution and translational temperature, the only two thermodynamical parameters required for the plasma fluid model, are plotted in the upper and lower panels, respectively.

of the potential follow the geometry of the jaws and decrease as a function of distance to the nozzle. The extent of the plasma sheath is around a few hundreds of micrometer from the jaws tip close to the flow axis and longer than 10 mm at the limit of the simulation in the y -axis ($y = 15 \text{ mm}$). The net positive charge density within the sheath leads to a potential profile that falls sharply from -1210 V near the cathode surface in the plasma region. This sheath confirms that the plasma is at steady condition.³² The electric potential upstream the anode plates is close to zero because of the nozzle geometry. The low absolute voltage potential (nearly zero volts) observed in the other regions is because the plasma is quasi-neutral, and thus, there is almost no net charge.

Out of the cathode fall region, within the residual gas of the vacuum chamber, the electric field intensity presents a relatively small gradient as can be seen in Fig. 6(b). In Fig. 6(c), the reduced electric field distribution indicates that the discharge is facilitated at steady-state condition in the plasma sheath area. Indeed, an intensity maximum can be found at the two angles of the jaws' geometry, which is due to a local field enhanced effect. These high electric field strength regions maintain the plasma without influencing the expansion. Low reduced electric field strength, observed inside the hollow and in a lesser extent within the isentropic core, arises mainly from the low electric field strength in these areas.

The increase in electrical intensity along the boundary in Figs. 6(b) and 6(c) beyond 12 mm from the nozzle output is the result from the boundary conditions, as described in Sec. III B.

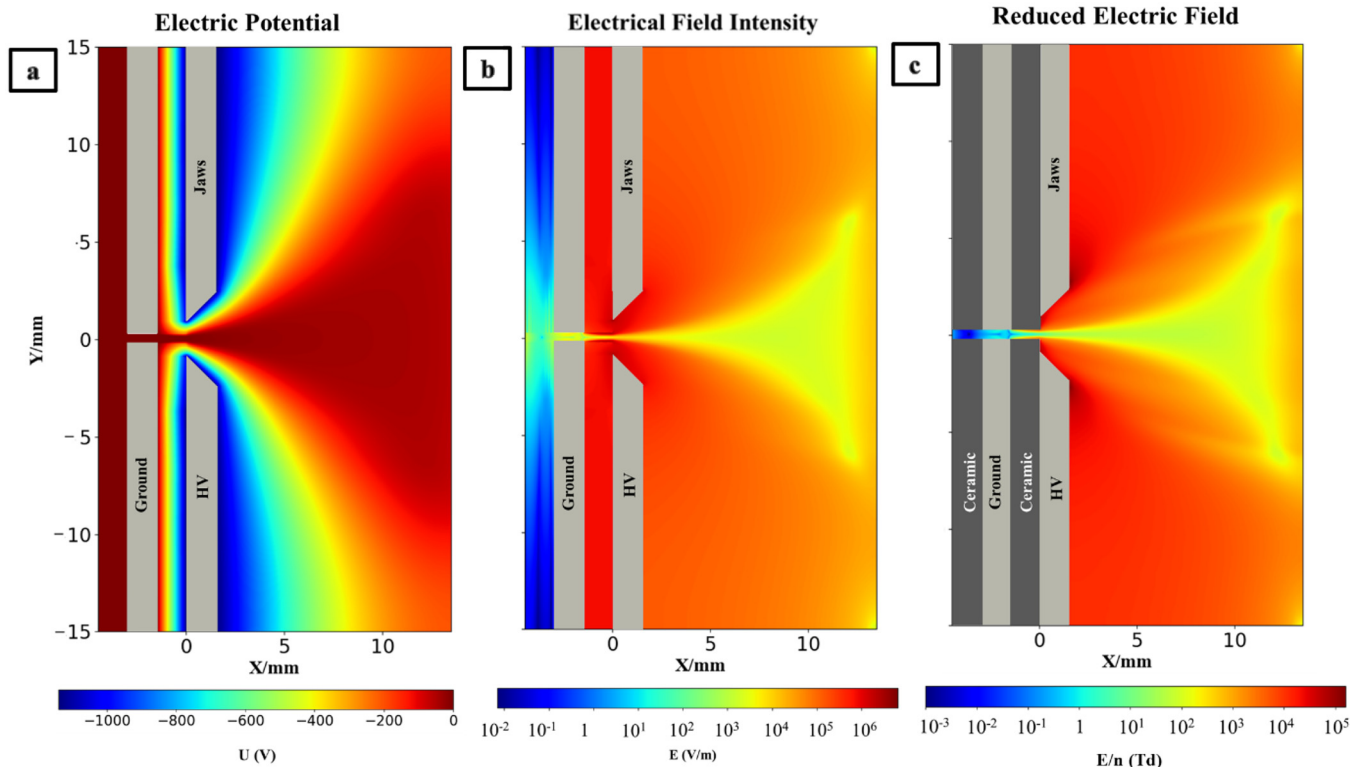


FIG. 6. Diagram showing (a) voltage potential, (b) electrical field intensity, and (c) reduced electric field at steady-state condition of -1400 V for the nozzle geometry and conditions as described in the text.

2. Particle density distributions and electron temperature

a. Electron density. The electron density distribution, presented in Fig. 7(a), shows a maximum along the flow axis between the cathode and anode referred to as the cathode–dielectric–anode (CDA) region. As mentioned earlier, the argon density inside the hollow is much higher than downstream from the nozzle orifice. Our simulation results highlight that a higher argon density increases the electron concentration due to the secondary emission of electrons produced by ionizing collisions. Thus, the electron density in that area is about one order of magnitude higher (10^{13} – 10^{14} cm^{-3}) than observed inside the isentropic core.

The presence of electrons upstream of the CDA region is due to a diffusion effect in the hollow, as there is no voltage potential to influence the electron displacement. The electron density in the cathode fall region is also very low as it is repelled by the electric field. In the isentropic core, the ionization rate drops as the electric field intensity and argon density decrease with the distance from the nozzle output. This also leads to a progressive reduction in the electron density (summarized in Fig. 7 showing n_e along the flow axis).

Compared with the previous studies on a similar setup by Broks *et al.*,¹⁷ our cathode jaws are shifted by 0.6 mm outward from the slit aperture of the dielectric plate, while in Broks *et al.*, it is the anode that

is shifted 0.1 mm inward. In both studies, the concentration of electrons is higher at the center of the CDA region, but this slight geometry difference modifies its distribution on the y -axis. In our study, this maximum is found on the flow axis, while in the case of Broks *et al.*, it lies closer to the insulator plate although our lower mesh resolution could explain this difference. Finally, if we restrain our comparison to the flow axis (x -axis) only shown in Fig. 7, the evolution of the electron density turns out to be maximum at 250 μm after and 700 μm before the nozzle output in Broks *et al.*¹⁷ and in our work, respectively.

b. Electron temperature. The electron temperature distribution shown in Fig. 7 corresponds to the mean electron energy. Within the cathode fall region, this electron temperature (around 100 eV) is much higher than any other regions. The electron temperature along the flow axis in the isentropic core of the plasma jet (the red line in Fig. 7) is around 4 eV, a typical value for a low-temperature plasma. Therefore, the ionization taking place within the isentropic core arises mainly from the excited argon states even if the fewer but higher energy electrons of the Boltzmann distribution are likely to directly ionize the argon from its ground state.

c. Ion density. Overall, along the flow axis, the number density of Ar^+ and its evolution is very similar to what has been observed for

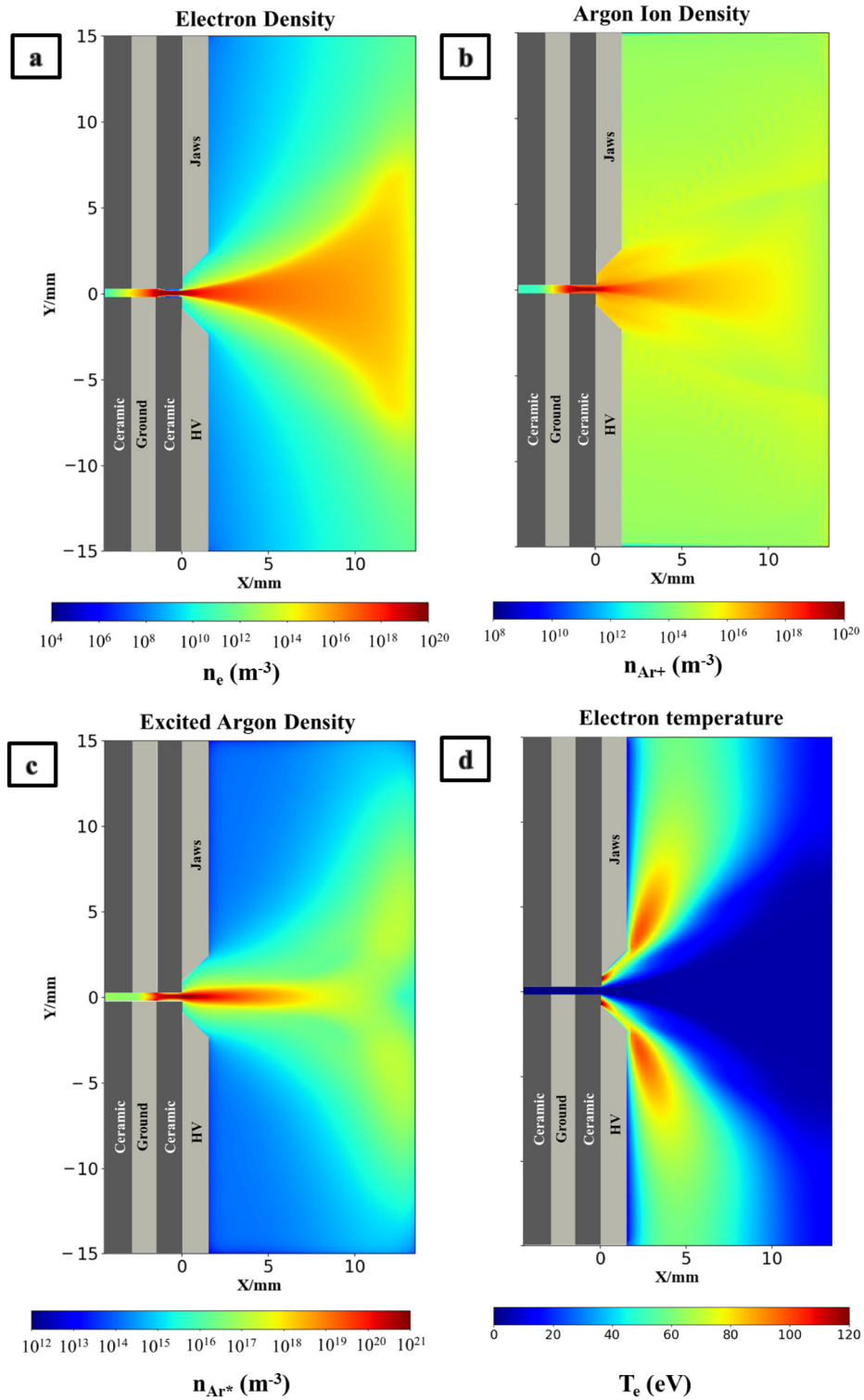


FIG. 7. (a) Electron, (b) argon cation, and (c) metastable argon densities' distribution along with (d) electron temperature a t steady-state condition.

04 June 2024 07:58:53

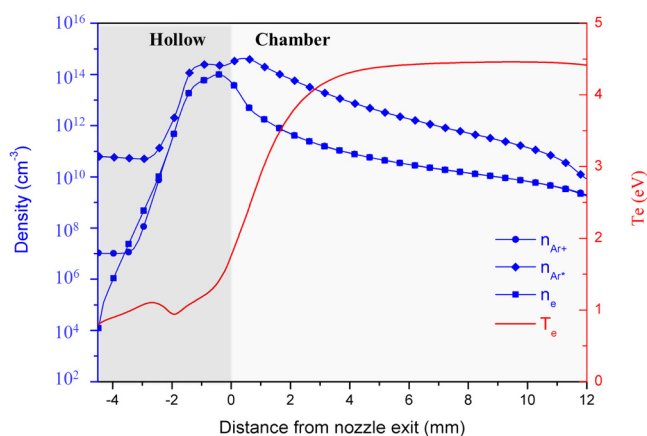


FIG. 8. Diagram showing the electron density (n_e), argon cation density (n_{Ar^+}), excited argon density (n_{Ar^*}), and electron temperature (T_e) along the flow axis extracted from the 2D distributions presented in Fig. 7.

the electrons [see Figs. 7(b) and 8]. Considering that Ar^+ is assumed to be the only cation present, this is directly linked to the conservation of space charge. The region upstream the CDA diverges from this trend by showing a higher cation density compared to its electron counterpart. This region is, in fact, associated with a constant Ar^+ density resulting from an electric force drift phenomenon. While the electrons are attracted to the anode surface, the Ar^+ is pushed away.

As mentioned above, the large difference between n_{Ar^+} and n_e in the sheath region is a result of a self-consistent electric field. Cations are concentrated to the cathode surface by the electric field force, while the electrons are repelled by this same force generated by the negative high-voltage cathode and move outward. Moreover, as the mass of an argon cation is orders of magnitude larger than that of an electron, the resulting velocity differences explain the existence of regions that are locally not neutral.

d. Excited argon density. The spatial distribution of Ar^* particles is presented in Fig. 7(c). Since Ar^* is not affected by the electric field, its distribution is influenced by the argon density and by electron temperature below the ionization threshold. Along the flow axis, compared to the charged species, the density of Ar^* decreases relatively slowly and remains more than two orders of magnitude higher (see Fig. 8). This finding is interesting as Ar^* is thought to play a major role in the first stage of chemical processes through the ionization of complex hydrocarbon by soft Penning ionization.¹⁴ The high number density of Ar^* in the CDA region and the beginning of the isentropic core provides sufficient number density for collisional reactions, which could explain the PDN efficiency in producing large number densities of various transient species.

V. EXPERIMENTAL DATA AND COMPARISON WITH SIMULATION

A. Spectrometer

The P²DN is mounted horizontally with its slit parallel to the optical axis to probe the plasma by means of optical emission

spectroscopy (OES). The distance between the slit and optical axis used here is 10 mm. The plasma is monitored in emission through a MgF_2 window, and light is collimated by two lenses before it enters a broadband spectrometer through an optical fiber. This Czerny–Turner-type spectrograph (Andor Shamrock SR-750) disperses the plasma emission by an 1800 lines/mm holographic grating offering 20 nm bandpass (covering 300–950 nm) with a resolution of 0.03 nm. Light is detected by a Newton CCD detector (2048 × 512 pixels of 13.5 μm). The spectrometer has been calibrated in spectral sensitivity and wavelength by Andor, and only small variations were noted over time. An optical mechanical shutter is positioned behind the exit window to guarantee that measurements are only taken during plasma operation in order to effectively increase the duty cycle (Fig. 9).⁹

During a measurement, the trigger of the valve is synchronized with the optical mechanical shutter and the pulsed power generator switch. The gas pulse is monitored by measuring the voltage on the electrodes. The characteristic voltage bump induced by the discharge over the expanding gas versus time is adjusted to coincide with the light signal detected by a separate photodiode for synchronization.¹⁰ The CCD camera gathers the emission from the plasma during 10 cycles of 20 s each to generate a spectrum. To reduce the contribution of ambient light and select only light generated by the plasma, the setup is fully shielded by black curtains during operation. It should be noted that the signal observed in this work originates from integration of a larger region in the plasma expansion. Basic *in situ* characterization showed that the OES collection area is a circular region with a radius of roughly 5 mm [see Fig. 1(c)], meaning that we integrate over different temperature and density regions. This size is determined by the aperture of the windows and the lens system and optics sending the light into the fiber and the center of this circular area coincide with one of the windows. In the case presented here, the light is collected 10 mm away from the nozzle output. The emission is recorded during the experiments in the stable discharge regime where the plasma dynamics process has reached a plateau, ensuring the plasma is probed in a steady-state condition.

B. Experimental results

Hereafter, the electron temperature and density derived from the model presented above are compared with experimental results obtained for different reservoir pressures. An experimental validation of the numerical approach will give confidence in the DSMC-extFM to reproduce accurately the supersonic plasma expansion generated in our lab and, thus, understand and optimize the physical process of such environments.

As mentioned above (see Sec. IV B 2), most of the processes are expected to occur inside the hollow. Although an accurate experimental characterization of this area is highly needed, the geometry and the size of the nozzle do not allow direct optical access. Thus, here the downstream emission spectra of supersonic expansion are used as a proxy to validate the numerical model and in turn to achieve indirectly a confidence verification of the plasma parameters in the CDA region. The electron temperature and density are two parameters playing a major role in the plasma

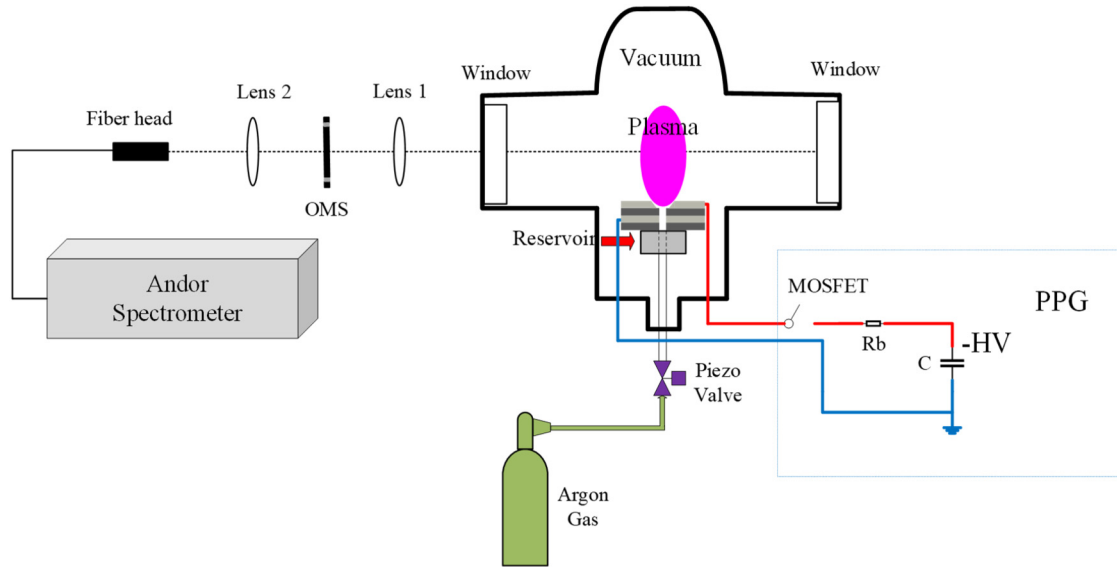


FIG. 9. Diagram of the experiment setup used in this work; Windows are made of MgF_2 ; OMS is the optical mechanical shutter; PPG is the pulse power generator; MOS is the metal–oxide–semiconductor field-effect transistor switch; Rb indicates the ballast resistor; C represents the set of capacitors. The red line represents the line connected to the negative high voltage output; the blue line represents the line grounding. The Andor spectrometer is used to disperse and detect the plasma emission.

environment, and if these are well reproduced, we expect that the distribution of excited and ionized argon will be valid as well.

To describe a plasma, different simplifications can be made depending on the ionization ratio and pressure of the environment. While at low pressure (<1 Pa) and ionization rate ($<10^{-5}$), a corona model is sufficient to describe the depopulation processes, through spontaneous radiation,⁵⁷ at higher pressure and ionization rate, where the depopulation of the excited states is dominated by the atom–electron collision reactions, a Boltzmann fitting is usually performed. In the current case, our plasma could not be sorted in either of these extreme simplifications and a complete collisional-radiative (CR) model is required to extract information from the emission spectra presented in Fig. 10.

The CR model developed here has been inspired by Zhu *et al.*³³ who introduced a well-described approach for low-temperature argon plasma based on the evaluation of the escape factor through a line-ratio method. This model remains relatively simple as it relies on a set of fundamental assumptions: the electron energy distribution function (EEDF) is described by a two-term Boltzmann equation and the density of excited species is assumed to be uniform across the measurement area. To further simplify the approach, here, only the 2p population distribution is used as solution of the rate balance equations of the CR model to retrieve the electron density and temperature. The 1s level densities, necessary to evaluate the 2p population processes, are determined through a line-ratio method.⁵⁸ Thus, the experimental determination of the electron temperature and density is a three-step process starting with the extraction of the 1s densities, then continues with the 2p relative populations and ends with adjusting the plasma parameter in the CR model to match the density of 2p levels as determined experimentally.

The direct determination of the 1s population concentration from the experimental spectra is made possible thanks to the reabsorption process occurring in most of the plasma environments (even at low pressure) via the concept of the escape factor.⁵⁹ Apart from the intrinsic characteristic of the transitions, such as the spontaneous emission coefficient and the degeneracy factors of the levels involved, this notion only depends on the density of the lower level and the gas temperature through the determination of the line shape that is dominated by the thermal agitation (Doppler broadening). As the gas temperature has already been estimated through a DSMC approach, only the density of the states involved is to be determined. A line ratio approach, based on choosing selected transitions to account for the different (de)excitation processes, is particularly useful to cancel out the unknown variables coming from the excited states (which will be treated in the next step). In this study, the set of line ratios is similar to those used in Ref. 60: $2p_8 \rightarrow 1s_5:2p_8 \rightarrow 1s_4$, $2p_6 \rightarrow 1s_4:2p_6 \rightarrow 1s_2$, $2p_3 \rightarrow 1s_5:2p_3 \rightarrow 1s_2$, $2p_3 \rightarrow 1s_4:2p_3 \rightarrow 1s_2$ and $2p_4 \rightarrow 1s_3:2p_4 \rightarrow 1s_2$. In addition to their relatively high intensity, these transitions are well isolated from other transitions that could disrupt their intensity determination. The 1s population distribution, thus, retrieved at different reservoir pressure conditions is depicted in Fig. 12(a).

The metastable and resonance states have been sorted together as they are sensitive to different excitation processes. The population of the metastable states increases according to the total density of the argon ground state except at 815 mbar, which will be discussed later in this article. The metastable populations are similar even if $1s_3$ is slightly more populated independent of the pressure. While the metastable states follow an expected behavior,⁶¹ the population of the resonance states show two unusual trends. First,

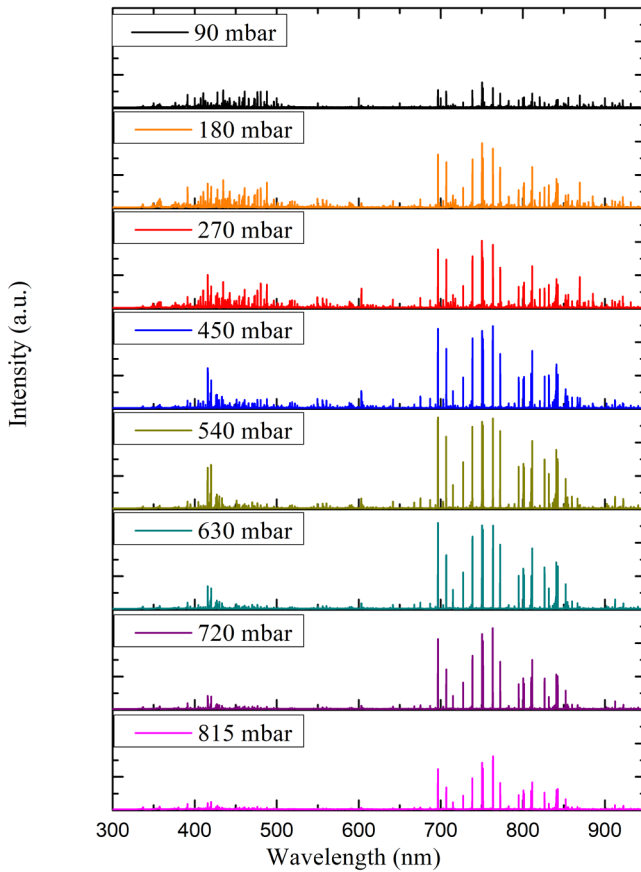


FIG. 10. Emission spectra of argon from the supersonic plasma expansion recorded 10 mm away from the nozzle output for seven different reservoir pressures (from 90 to 815 mbar).

although their excitation processes are similar, the $1s_2$ level is clearly more populated than $1s_4$. Second, as the pressure increases, the radiative decay should be counterbalanced by the trapping effect leading to an increase in their population with respect to the metastable states.⁶² Yet, here the resonant state densities remain stable over the pressure range studied in this paper. Although further investigation is required to understand this observation, an uneven population distribution within the resonance levels may hint to a non-steady state as the $1s$ levels adapt slowly to change of electron temperature.⁶³

These $1s$ densities are then used to determine the relative ones of the $2p$ states through a line-ratio approach where a least squares method is used to solve a system of 109 equations, including all the workable $2p$ to $1s$ transitions that we could retrieve from the spectrum shown in Fig. 11. As for the $1s$ populations, the $2p$ relative densities, shown in Fig. 12, associated with different reservoir pressures, are sorted in different groups according to their sensitivities to the (de-)excitation processes.³³ The first group includes $2p_1$ and $2p_5$ levels that are associated with large electron impact excitation

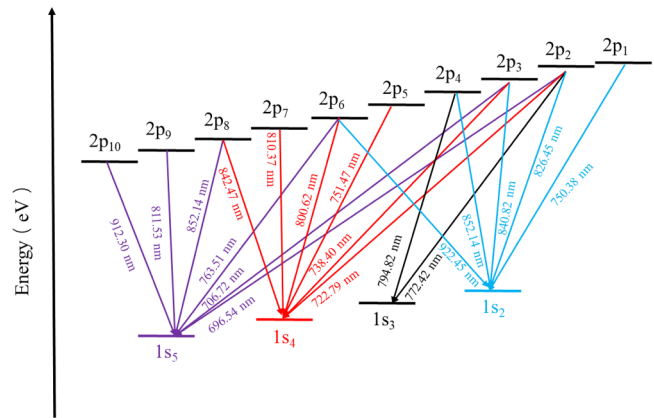


FIG. 11. The optical transitions used in the collisional-radiative model in this work. The arrows refer to the optical transitions.

rate coefficients per degeneracy degree from the ground state. The decrease in their population (especially for $2p_1$) over the pressure (except at 815 mbar) relative to the other groups is directly related to the diminution of the electron temperature. The second ($2p_3$, $2p_7$, and $2p_8$) and third ($2p_4$ and $2p_9$) groups present a large excitation rate coefficient from the resonance and metastable energy levels, respectively. Their evolution, as function of the pressure, follows their corresponding $1s$ levels. The group linked to the resonance levels remains rather unchanged, while the one related to the metastable states sees its population increasing. The last set of $2p$ levels includes $2p_2$, $2p_6$, and $2p_{10}$ and is characterized by relatively small atomic collision population transfer rate coefficients.³⁴ Overall, in the $2p$ population distributions of our plasma, the $2p_1$ level shows the largest population, which clearly differs from well-characterized plasma such as EBP,³³ ICP,³⁴ CCP,³⁵ and SRR.³⁶ As $2p_1$ is associated with a relatively high electron impact excitation rate coefficient from the ground state compared to the other excitation pathway, this suggests that, in P^2 DN system, the ground-state excitation is the dominant process.

The distribution and evolution over the pressure range of the population in the four $2p$ levels groups indicate the complexity of the dynamic process in our supersonic plasma expansion and mainly result from the evolution of the electron temperature and to a lesser extent from the density.

These $2p$ population distributions are used as the solution of the rate balance equation where the electron temperature and density are determined through a least square method. The rate balance equation includes all the main (de)excitation processes observed in a plasma except the ionization pathways and atomic collisions that are both negligible in our pressure (~ 10 Pa) and ionization ratio ($\sim 10^{-7}$) conditions. Thus, the CR model includes the electron impact (de)excitation involving the ground state, $1s$ and $2p$ levels, and electron impact population transfer between $2p$ and $2s3d$ levels, along with the radiation decay and trapping effect. In fact, as the absolute density of the $2p$ levels is required to describe some of the excitation process, the CR model proceeds in two

04 June 2024 07:58:53

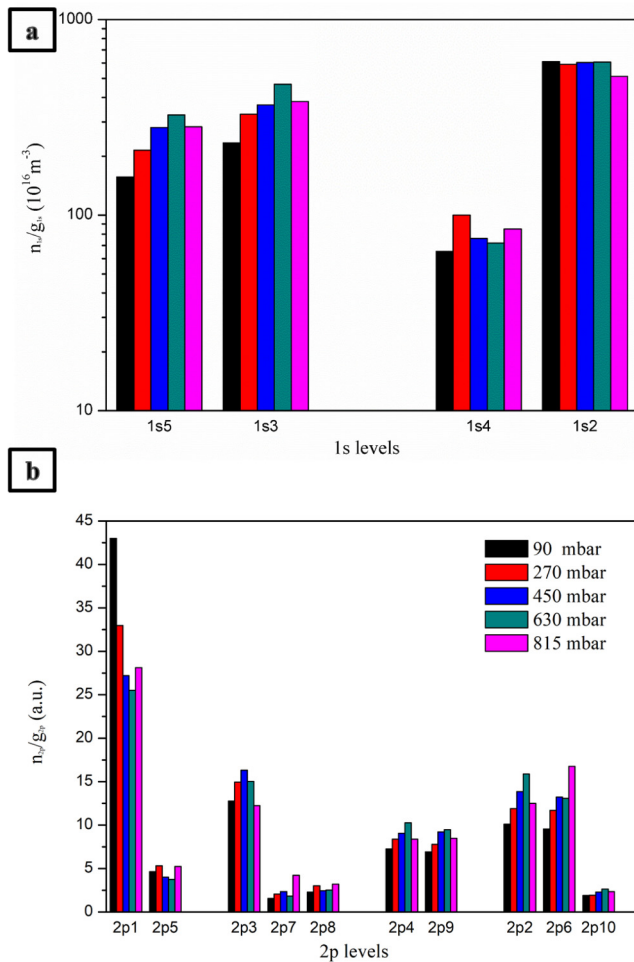


FIG. 12. Population distribution of 1s and 2p levels from the OES measurement for five different reservoir pressures. n and g are the population density and the degeneracy degree of the designated levels. The values of n_{2p}/g_{2p} are normalized to 100.

steps. A first estimation of the electron temperature and density is used to obtain a good guess of the density of the 2p states, and then, these densities are used in the model to recalculate the best fit for the electron density and temperature. The process is repeated until the parameters have reached the convergence criteria.

As shown in Fig. 13, the electron temperature retrieved from the experimental spectra through the collisional-radiative model is in good agreement with the plasma simulation based on an extended fluid model although it is slightly underestimated by the simulation at high reservoir pressures. Only electron temperature associated with a 815 mbar reservoir pressure show clear divergence from the model, which is related to the non-realistic population distribution of 1s population (and in consequence to the 2p distribution also). Brief variation in our experimental conditions may have impaired the data collection for this specific point.

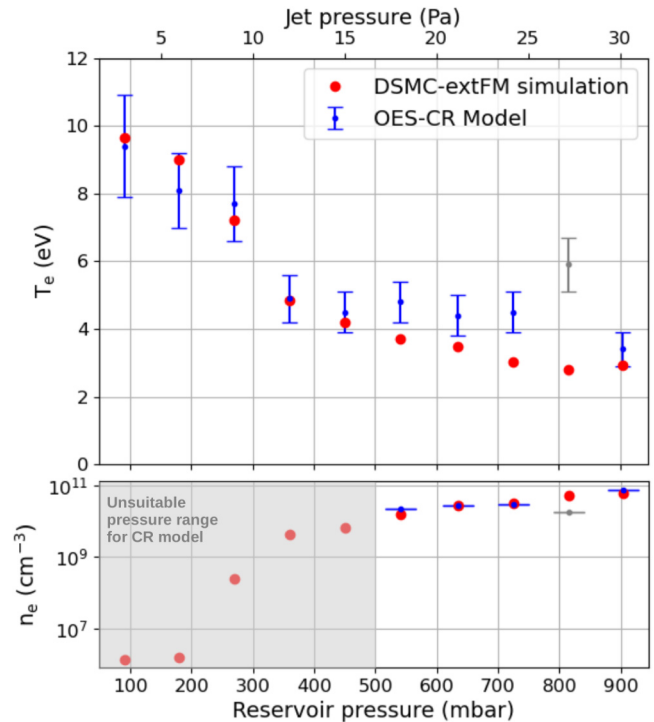


FIG. 13. Synthetic (red) and experimental (blue) evolutions of (a) electron temperature T_e and (b) electron density n_e for different reservoir pressures at a position 10 mm away from the nozzle output.

Skipping the evaluation of the 1s population inside our CR model leads to another drawback. In the low-pressure condition, the model becomes insensitive to the electron density as all the main excitation processes are proportional to this density.⁶³ Thus, the densities provided by the CR model are unrealistic below 450 mbar reservoir pressure. The better agreement between the numerical and experimental characterization for the electron density at higher pressures is due to the electron impact population transfer, which is no longer negligible for the lowest energy levels of the 2p manifold. It should be noted that due to its lower importance in the 2p population fitting, the electron density uncertainty given by the code is unrealistically low and the overall uncertainty of the characterization is in fact fully held by the electron temperature as both parameters are evaluated in parallel.

From these findings, we conclude that the main process turns out to be the electron impact excitation from the lower levels (ground state and 1s levels), while the electron impact population transfer only plays a role at the higher pressures studied here. The de-excitation by radiation tends to be compensated by radiation trapping in our pressure range. As expected, the electron temperature decreases as the pressure increases, but this temperature is still high enough to ionize the more abundant neutral gas in a two-step process leading to an increase in electron density.

This simple CR model is sufficient to validate our numerical approach. Further improvements are possible, though, and would

04 June 2024 07:58:53

need to address the 1s excitation step within the CR model to deal with the unrealistic electron density at low pressure. A better accuracy could be reached by taking into account the non-uniform distribution of the excited species over the volume covered by the spectrometer. For this purpose, another approach that eliminates the escape factor could be implemented.⁶⁴ Finally, adding currently missing kinetic processes may enable a more accurate description of the (de)excitation processes even under higher pressure conditions. Experimentally, a time-dependent study of the evolution of the 1s population through a line-ratio method may explain the unusual distribution of the resonance states populations, which, in turn, could enhance the numerical approach by following the kinetics during a gas pulse.

V. CONCLUSION

In this study, we have developed a numerical approach to simulate a micro-hollow cathode discharge coupled with supersonic Argon expansion. The association of a plasma extended fluid model with a direct simulation Monte Carlo to describe the rarefied gas leads to parameters of the plasma at any location of the flow. In parallel, a homemade collisional-radiative model allowed for extracting the electron temperature and density from experimental spectra recorded through emission spectroscopy, sampling the plasma region downstream of the orifice inside the vacuum chamber. The supersonic plasma is produced in the lab with an updated version of an established plasma expansion setup (P²DN) using a piezostack valve allowing for an accurate control of the reservoir pressure. A good agreement between the *in situ* observations and its synthetic counterparts is found over a wide range of pressures. Only the electron density at low reservoir pressure (<500 mbar) diverges from the numerically expected values. This expected discrepancy arises from an inherent weakness of our CR model, which will be addressed in a future work. These experimental findings in line with the numerical results give an assuring degree of confidence about the entire approach and, thus, lead, in particular, to a better understanding of the conditions within the hollow, a crucial region for using such apparatus for complex hydrocarbon chemistry studies. Indeed, the simulation highlighted that in our typical operating conditions (−1400 V and 2 k Ω ballast resistor), the maximum densities of electrons and ions occur right before the nozzle output while the densest region for the excited neutral species lies right after this aperture. The numerical approach presented in this article will be used to better understand the complex chemistry occurring within this type of supersonic plasma when adding reactive precursors to the expansion. The ultimate goal is to subsequently optimize plasma conditions for the formation of new transient species of astrophysical interest, such that they can be spectroscopically characterized.

ACKNOWLEDGMENTS

This work was supported by China Scholarship Council, the Netherlands Organization for Scientific Research through a VIDI Grant (No. 723.016.006) and a VICI Grant (No. 639.043.905) as well as by the National Natural Science Foundation of China (NNSFC) (Nos. U1537210 and 51277147).

AUTHOR DECLARATIONS

Conflict of Interest

The authors have no conflicts to disclose

Author Contributions

Yu Gu: Data curation (equal); Formal analysis (equal); Investigation (equal); Software (equal); Visualization (equal); Writing – original draft (equal). **Nicolas Suas-David:** Conceptualization (lead); Data curation (equal); Formal analysis (equal); Investigation (lead); Methodology (lead); Software (lead); Validation (lead); Visualization (equal); Writing – original draft (equal). **Jordy Bouwman:** Funding acquisition (equal); Methodology (equal); Supervision (supporting); Validation (equal); Writing – review & editing (equal). **Yongdong Li:** Funding acquisition (equal); Methodology (equal); Supervision (equal); Validation (equal); Writing – review & editing (equal). **Harold Linnartz:** Funding acquisition (equal); Methodology (equal); Supervision (lead); Validation (equal); Writing – review & editing (equal).

DATA AVAILABILITY

The data that support the findings of this study are available from the corresponding author upon reasonable request.

REFERENCES

- ¹T. F. Giesen, A. Van Orden, H. Hwang, R. Fellers, R. Provencal, and R. Saykally, “Infrared laser spectroscopy of the linear C₁₃ carbon cluster,” *Science* **265**, 756–759 (1994).
- ²P. Neubauer-Guenther, T. F. Giesen, U. Berndt, G. Fuchs, and G. Winnewisser, “The Cologne carbon cluster experiment: Ro-vibrational spectroscopy on C₈ and other small carbon clusters,” *Spectrochim. Acta A* **59**, 431–441 (2003).
- ³M. Fukushima, M.-C. Chan, Y. Xu, A. Taleb-Bendiab, and T. Amano, “High-resolution infrared absorption spectroscopy of jet-cooled molecular ions,” *Chem. Phys. Lett.* **230**, 561–566 (1994).
- ⁴D. T. Anderson, S. Davis, T. S. Zwier, and D. J. Nesbitt, “An intense slit discharge source of jet-cooled molecular ions and radicals (Trot & 30 K),” *Chem. Phys. Lett.* **258**, 207–212 (1996).
- ⁵T. Motylewski and H. Linnartz, “Cavity ring down spectroscopy on radicals in a supersonic slit nozzle discharge,” *Rev. Sci. Instrum.* **70**, 1305–1312 (1999).
- ⁶D. Pfluger, W. E. Sinclair, H. Linnartz, and J. P. Maier, “Rotationally resolved electronic absorption spectra of triacetylene cation in a supersonic jet,” *Chem. Phys. Lett.* **313**, 171–178 (1999).
- ⁷H. Linnartz, D. Verdes, and T. Speck, “High resolution infrared direct absorption spectroscopy of ionic complexes,” *Rev. Sci. Instrum.* **71**, 1811–1815 (2000).
- ⁸D. Zhao, M. A. Haddad, H. Linnartz, and W. Ubachs, “C₆H and C₆D: Electronic spectra and Renner-Teller analysis,” *J. Chem. Phys.* **135**, 044307 (2011).
- ⁹A. Walsh, D. Zhao, W. Ubachs, and H. Linnartz, “Optomechanical shutter modulated broad-band cavity-enhanced absorption spectroscopy of molecular transients of astrophysical interest,” *J. Phys. Chem. A* **117**, 9363–9369 (2013).
- ¹⁰A. J. Walsh, D. Zhao, and H. Linnartz, “Note: Cavity enhanced self-absorption spectroscopy: A new diagnostic tool for light emitting matter,” *Rev. Sci. Instrum.* **84**, 026108 (2013).
- ¹¹H. Linnartz, D. Verdes, and J. P. Maier, “Rotationally resolved infrared spectrum of the charge transfer complex [Ar-N₂]⁺,” *Science* **297**, 1166–1167 (2002).
- ¹²G. Bazalgette Courrèges-Lacoste, J. P. Sprengers, J. Bulthuis, S. Stolte, T. Motylewski, and H. Linnartz, “Vibrationally excited state spectroscopy of radicals in a supersonic plasma,” *Chem. Phys. Lett.* **335**, 209–214 (2001).

- ¹³D. Romanini, L. Biennier, F. Salama, A. Kachanov, L. J. Allamandola, and F. Stoeckel, "Jet-discharge cavity ring-down spectroscopy of ionized polycyclic aromatic hydrocarbons: Progress in testing the PAH hypothesis for the diffuse interstellar band problem," *Chem. Phys. Lett.* **303**, 165–170 (1999).
- ¹⁴L. Biennier, F. Salama, L. J. Allamandola, and J. J. Scherer, "Pulsed discharge nozzle cavity ringdown spectroscopy of cold polycyclic aromatic hydrocarbon ions," *J. Chem. Phys.* **118**, 7863–7872 (2003).
- ¹⁵S. E. Fiedler, A. Hese, and A. A. Ruth, "Incoherent broad-band cavity-enhanced absorption spectroscopy," *Chem. Phys. Lett.* **371**, 284–294 (2003).
- ¹⁶B. H. P. Broks, W. J. M. Brok, J. Remy, J. J. A. M. van der Mullen, A. Benidar, L. Biennier, and F. Salama, "Modeling the influence of anode–cathode spacing in a pulsed discharge nozzle," *Spectrochim. Acta, Part B*, **60**, 1442–1449 (2005).
- ¹⁷B. H. P. Broks, W. J. M. Brok, J. Remy, J. J. A. M. van der Mullen, A. Benidar, L. Biennier, and F. Salama, "Numerical investigation of the discharge characteristics of the pulsed discharge nozzle," *Phys. Rev. E* **71**, 036409 (2005).
- ¹⁸J. Remy, L. Biennier, and F. Salama, "Plasma structure in a pulsed discharge environment," *Plasma Sources Sci. Technol.* **12**, 295 (2003).
- ¹⁹C.-H. Chang, J. Agarwal, W. D. Allen, and D. J. Nesbitt, "Sub-Doppler infrared spectroscopy and formation dynamics of triacetylene in a slit supersonic expansion," *J. Chem. Phys.* **144**, 074301 (2016).
- ²⁰F. T. Giesen, E. M. Harding, J. Gauss, J.-U. Grabow, and H. S. P. Müller, "Determination of accurate rest frequencies and hyperfine structure parameters of cyanobutadiyne, HC5N," *J. Mol. Spectrosc.* **371**, 111303 (2020).
- ²¹H. Linnartz, D. Pfluger, O. Vaizert, P. Cias, P. Birza, D. Khoroshev, and J. P. Maier, "Rotationally resolved A2Πu←X 2Πg electronic transition of NC6N⁺," *J. Chem. Phys.* **116**, 924–927 (2002).
- ²²R. H. Stark and K. H. Schoenbach, "Direct current high-pressure glow discharges," *J. Appl. Phys.* **85**, 2075–2080 (1999).
- ²³K. H. Schoenbach and K. Becker, "20 years of microplasma research: A status report," *Eur. Phys. J. D* **70**, 29 (2016).
- ²⁴D. Levko, E. Krasik Ya, V. Vekselman, and I. Haber, "Two-dimensional model of orificed micro-hollow cathode discharge for space application," *Phys. Plasmas* **20**, 083512 (2013).
- ²⁵L. Kong, W. Wang, A. B. Murphy, and G. Xia, "Numerical analysis of direct-current microdischarge for space propulsion applications using the particle-in-cell/monte carlo collision (PIC/MCC) method," *J. Phys. D: Appl. Phys.* **50**, 165203 (2017).
- ²⁶Q. Han, S.-X. Gao, J. Wang, W.-P. Shu, and L.-Z. Zhang, "Electron heating mechanism in radio-frequency microhollow cathode discharge in nitrogen," *Phys. Plasmas* **24**, 063509 (2017).
- ²⁷X. Li, C. Ren, X. He, K. Wu, P. Jia, and S. Li, "Influence of operating parameters on high-pressure microhollow cathode discharge with a cylindrical hole," *Plasma Process Polym.* **17**, 1900228 (2020).
- ²⁸H. Wei, N. Wang, Z. Duan, and F. He, "Experimental and simulation study of pulsed micro-hollow cathode discharge in atmospheric-pressure helium," *Physics of Plasmas* **25**(12), 2018.
- ²⁹X.-X. Jiang, F. He, Q. Chen, T. Ge, and J.-T. Ouyang, "Numerical simulation of the sustaining discharge in radio frequency hollow cathode discharge in argon," *Phys. Plasmas* **21**, 033508 (2014).
- ³⁰C. Lazzaroni and P. Chabert, "A global model of micro-hollow cathode discharges in the stationary regime," *J. Phys. D: Appl. Phys.* **44**, 445202 (2011).
- ³¹C. Lazzaroni and P. Chabert, "A global model of the self-pulsing regime of micro-hollow cathode discharges," *J. Appl. Phys.* **111**, 053305 (2012).
- ³²B. H. P. Broks, W. J. M. Brok, J. Remy, J. J. A. M. van der Mullen, A. Benidar, L. Biennier, and F. Salama, "Modeling the influence of anode–cathode spacing in a pulsed discharge nozzle," *Spectrochim. Acta, Part B*, **60**, 1442–1449 (2005).
- ³³X.-M. Zhu and Y.-K. Pu, "A simple collisional–radiative model for low-temperature argon discharges with pressure ranging from 1 Pa to atmospheric pressure: Kinetics of Paschen 1s and 2p levels," *J. Phys. D: Appl. Phys.* **43**, 015204 (2010).
- ³⁴X.-M. Zhu and Y.-K. Pu, "A simple collisional–radiative model for low-pressure argon discharges," *J. Phys. D: Appl. Phys.* **40**, 2533–2538 (2007).
- ³⁵X.-M. Zhu, W.-C. Chen, S. Zhang, Z.-G. Guo, D.-W. Hu, and Y.-K. Pu, "Electron density and ion energy dependence on driving frequency in capacitively coupled argon plasmas," *J. Phys. D: Appl. Phys.* **40**, 7019–7023 (2007).
- ³⁶F. Iza and J. Hopwood, "Split-ring resonator microplasma: Microwave model, plasma impedance and power efficiency," *Plasma Sources Sci. Technol.* **14**, 397–406 (2005).
- ³⁷K. Kano, M. Suzuki, and H. Akatsuka, "Spectroscopic measurement of electron temperature and density in an argon plasma jet based on collisional-radiative model," *Contrib. Plasma Phys.* **41**, 91–102 (2001).
- ³⁸C. Abeysekera, B. Joalland, Y. Shi, A. Kamasah, J. M. Oldham, and A. G. Suits, "Note: A short-pulse high-intensity molecular beam valve based on a piezoelectric stack actuator," *Rev. Sci. Instrum.* **85**, 116107 (2014).
- ³⁹G. A. Bird, *Molecular Gas Dynamics and the Direct Simulation of Gas Flows* (Oxford University Press, 1994).
- ⁴⁰G. A. Bird, "The DS2V/3V program suite for DSMC calculations," *AIP Conf. Proc.* **762**, 541–546 (2005).
- ⁴¹A. Lietard, G. Gallician, J. Tan, M.-A. Gaveau, M. Briant, B. Soep, J.-M. Mestdagh, and L. Poisson, "Characterisation and modeling of a pulsed molecular beam," *Mol. Phys.* **119**, e1737743 (2021).
- ⁴²D. Pentlechner, R. Riechers, B. Dick, A. Slenczka, U. Even, N. Lavie, R. Brown, and K. Luria, "Rapidly pulsed helium droplet source," *Rev. Sci. Instrum.* **80**, 043302 (2009).
- ⁴³V. Casseau, *Github Repository of the Hystrath Platform* (Github, 2020).
- ⁴⁴H. G. Weller, G. Tabor, H. Jasak, and C. Fureby, "A tensorial approach to computational continuum mechanics using object-oriented techniques," *Comput. Phys.* **12**, 620 (1998).
- ⁴⁵C. White, M. K. Borg, T. J. Scanlon, S. M. Longshaw, B. John, D. R. Emerson, and J. M. Reese, "Dsmcfoam+: An OpenFOAM based direct simulation Monte Carlo solver," *Comput. Phys. Commun.* **224**, 22–43 (2018).
- ⁴⁶C. K. Birdsall and D. Fuss, "Clouds-in-clouds, clouds-in-cells physics for many-body plasma simulation," *J. Comput. Phys.* **3**, 494–511 (1969).
- ⁴⁷L. Yongdong, H. Feng, and L. Chunliang, "A volume-weighting cloud-in-cell model for particle simulation of axially symmetric," *Plasma Plasma Sci. Technol.* **7**, 2653–2656 (2005).
- ⁴⁸E. Gogolides and H. H. Sawin, "Continuum modeling of radio-frequency glow discharges. I: Theory and results for electropositive and electronegative gases," *J. Appl. Phys.* **72**, 3971–3987 (1992).
- ⁴⁹I. Rafatov, E. A. Bogdanov, and A. A. Kudryavtsev, "On the accuracy and reliability of different fluid models of the direct current glow discharge," *Phys. Plasmas* **19**, 033502 (2012).
- ⁵⁰D. W. Pepper and J. C. Heinrich, *The Finite Element Method: Basic Concepts and Applications with MATLAB, MAPLE, and COMSOL* (CRC Press, 2017).
- ⁵¹G. J. M. Hagelaar and L. C. Pitchford, "Solving the Boltzmann equation to obtain electron transport coefficients and rate coefficients for fluid models," *Plasma Sources Sci. Technol.* **14**, 722 (2005).
- ⁵²G. Auday, P. Guillot, J. Galy, and H. Brunet, "Experimental study of the effective secondary emission coefficient for rare gases and copper electrodes," *J. Appl. Phys.* **83**, 5917–5921 (1998).
- ⁵³A. V. Phelps, L. C. Pitchford, C. Pédoussat, and Z. Donkó, "Use of secondary-electron yields determined from breakdown data in cathode-fall models for Ar," *Plasma Sources Sci. Technol.* **8**, B1–B2 (1999).
- ⁵⁴S. Mouchtouris and G. Kokkoris, "A hybrid model for low pressure inductively coupled plasmas combining a fluid model for electrons with a plasma-potential-dependent energy distribution and a fluid-Monte Carlo model for ions," *Plasma Sources Sci. Technol.* **25**, 025007 (2016).
- ⁵⁵Anon, *Atomic and Molecular Beam Methods* (Oxford University Press, 1988).
- ⁵⁶M. A. Lieberman and A. J. Lichtenberg, *Principles of Plasma Discharges and Materials Processing* (John Wiley & Sons, 2005).
- ⁵⁷X.-M. Zhu and Y.-K. Pu, "Optical emission spectroscopy in low-temperature plasmas containing argon and nitrogen: Determination of the electron temperature and density by the line-ratio method," *J. Phys. D: Appl. Phys.* **43**, 403001 (2010).

- ⁵⁸M. Schulze, A. Yanguas-Gil, A. von Keudell, and P. Awakowicz, "A robust method to measure metastable and resonant state densities from emission spectra in argon and argon-diluted low pressure plasmas," *J. Phys. D: Appl. Phys.* **41**, 065206 (2008).
- ⁵⁹H. R. Griem, *Principles of Plasma Spectroscopy* (Cambridge University Press, 2005).
- ⁶⁰J. Li, X.-M. Zhu, and Y.-K. Pu, Investigation on the atomic density of metastable and resonant levels in inductively coupled argon plasma (2009), see <https://www.semanticscholar.org/paper/Investigation-on-the-atomic-density-of-metastable-Li-Zhu/49a96736a5ea1fc790810f97a0eab71d5319581e#cite=1>
- ⁶¹J. Peshl, R. McNeill, C. I. Sukenik, M. Nikolić, S. Popović, and L. Vüsković, "Argon metastable and resonant level densities in Ar and Ar/Cl₂ discharges used for the processing of bulk niobium," *J. Appl. Phys.* **126**, 103302 (2019).
- ⁶²J. Li, X.-M. Zhu, and Y.-K. Pu, "The population distribution of argon atoms in Paschen 1s levels in an inductively coupled plasma," *J. Phys. D: Appl. Phys.* **43**, 345202 (2010).
- ⁶³J. Kaupe, D. Coenen, and S. Mitic, "Phase-resolved optical emission spectroscopy of a transient plasma created by a low-pressure dielectric barrier discharge jet," *Plasma Sources Sci. Technol.* **27**, 105003 (2018).
- ⁶⁴X.-M. Zhu, T. V. Tsankov, D. Luggenhölscher, and U. Czarnetzki, "2D collisional-radiative model for non-uniform argon plasmas: With or without 'escape factor'," *J. Phys. D: Appl. Phys.* **48**, 085201 (2015).